INTERNATIONAL JOURNAL OF HYDROGEN ENERGY 45 (2020) 26583–26594

Available online at www.sciencedirect.com

ScienceDirect

journal homepage: www.elsevier.com/locate/he

Ultralow loading electroless deposition of IrO_x on nickel foam for efficient and stable water oxidation catalysis

Rachela G. Milazzo [a], *Stefania M.S. Privitera* [a,*], *Silvia Scalese* [a], *Francesca Monforte* [a,b], *Corrado Bongiorno* [a], *Guglielmo G. Condorelli* [b], *Salvatore A. Lombardo* [a]

[a] *Consiglio Nazionale delle Ricerche (CNR), Istituto per la Microelettronica e Microsistemi (IMM), Zona Industriale VIII Strada 5, 95121, Catania, CT, Italy*

[b] *Dipartimento di Scienze Chimiche, Università di Catania and INSTM UdR Catania, Viale Andrea Doria 6, 95125, Catania, Italy*

HIGHLIGHTS

- IrO_x deposited on Ni foam by galvanic displacement followed by annealing in air.
- The electrode surface can be completely covered by IrO_x nanoparticles.
- Ni foam covered by IrO_x exhibits excellent catalytic activity and stability.
- Ir amount is about 35 μg cm^{-2}, well below typical values in PEM based fuel cells.

GRAPHICAL ABSTRACT

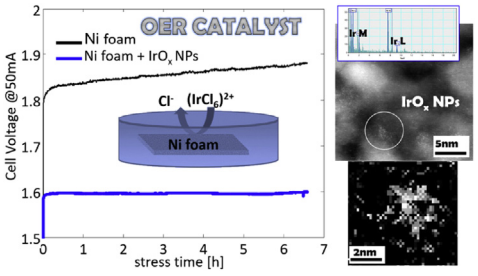

ARTICLE INFO

Article history:
Received 6 May 2020
Received in revised form
22 June 2020
Accepted 6 July 2020
Available online 31 July 2020

Keywords:
Water splitting
Hydrogen production
Anode electrocatalyst

ABSTRACT

Photocatalysis and electrolysis are crucial processes for the development of a sustainable, clean energy system, since they enable solar fuel production, such as hydrogen by water splitting, as well as CO_2 reduction. In these processes efficient and robust catalysts for water oxidation are required and the reduction of employed amount of noble metals is crucial to reduce costs and increase the sustainability of the technology. To obtain extremely low iridium loading on nickel foam electrodes we have employed electroless deposition by spontaneous galvanic displacement as a simple, low cost, highly scalable technique. After deposition the Ir oxidation has been achieved by annealing in air at 250 °C. By varying the deposition parameters, an optimal condition has been achieved, with an overpotential for water oxidation of 360 mV at 10 mA cm^{-2} in 1.0 M KOH solution. The Ni foam coverage with Ir oxide has also a positive impact on the electrode stability, strongly decreasing the degradation rate, compared to the case of bare Ni foam. The average

* *Corresponding author.*
E-mail address: stefania.privitera@imm.cnr.it (S.M.S. Privitera).

https://doi.org/10.1016/j.ijhydene.2020.07.049

Renewable energy
Noble metals nanoparticles

amount of noble metal in the best performing electrode is only 35 μg cm^{-2} for a 1.6 mm thick Ni foam electrode. The proposed approach is highly promising for gas diffusion electrodes, and can be implemented in electrolytic cells, as well as in fuel cells.

Introduction

Hydrogen can potentially be used in highly efficient fuel cells for transportation, in internal combustion engines, and as an energy carrier and storage medium. Today, hydrogen is most commonly used as an industrial feedstock for refineries and ammonia production in fertilizer industries. The main production is still from fossil fuels, whilst in a sustainable economy [1–5] it is recommended to produce hydrogen by water electrolysis driven by renewable energy sources. However, although promising, hydrogen generation by water splitting still needs to be improved in terms of efficiency and durability to become economically appealing [6,7]. Electrolytic cells can operate both at low (below 100 °C) and at high temperatures and with different ionic agents (OH^-, H^+ or O^-) depending on the electrolysis technologies, i.e., alkaline (AEC), polymer electrolyte membrane (PEM) or solid oxide electrolysis (SOE) [8–13]. Each of them has its drawbacks and advantages [14–17]. PEMs are among the most efficient devices but require high loading of platinum-based (Pt) noble metal catalysts (typically not lower than 0.1 mg cm^{-2}) [18–21] to drive the desired electrochemical reactions at the cathode, the hydrogen evolution reaction (HER). An even higher amount of rare and expensive materials such as Ir or Ru (in the range 1–4 mg cm^{-2}), is required for the oxygen evolution reaction (OER) at the anode. Indeed, the water oxidation occurring at the anode, with a sluggish kinetics, is considered the bottleneck in the electrochemical water splitting [22–26]. The reduction of the amount of noble and rare materials is therefore a key factor to maintain the cost low while increasing the sustainability. As an example, the U.S. Department of Energy (DOE) for the PEM based fuel cells is targeting a total Pt group loading of 0.125 mg cm^{-2} by 2020, to meet cost requirements [27,28]. This must be achieved while maintaining acceptable performance, stability, and durability.

To reduce the noble metal amount, an efficient way can be the use of a 3-D structured low cost and earth abundant electrodes, such as Carbon or Nickel, which allow high specific surface area and exhibit macro-pores beneficial for the electrolyte penetration and gas diffusion [29–36]. Here we incorporate an extremely low loading of Ir oxide onto a Ni foam to be used as gas diffusion electrode for the oxygen evolution reaction [37].

The strategies currently adopted for IrO_2 deposition include *in situ* growth through electrodeposition, hydrothermal methods, direct coating or sputtering of as prepared electro-catalysts. There are some papers reporting the fabrication of IrO_2 nanoparticles by Sol Gel processing [38], by the Adam's fusion method [39], by condensation [40,41], by electrodeposition [42–44] and involving high temperatures and/or long-time processes. IrO_2 can be also deposited by chemical vapor deposition techniques including PE-MOCVD (Plasma Enhanced Metal Organic CV) [45–48], DC magnetron sputtering [49], Radio Frequency Magnetron Sputtering [50], Atomic Layer Deposition (ALD) [51]. However, the afore mentioned techniques require high temperature (200–1000 °C), high purity precursors and/or complex experimental set up. Moreover, in some cases it might not be possible to achieve a complete and uniform coverage of a 3D structured electrode or to upscale the deposition.

In a previous work we have demonstrated that very low Pt loading (15 μg cm^{-2}) [52] can be successfully achieved by electroless galvanic displacement on nickel foam with a negligible cost increase, but with big advantages in terms of onset voltage and stability. In particular, the comparison with other deposition techniques has shown that the complete and uniform coverage is a key factor to improve the stability. In this paper we propose the galvanic displacement deposition, followed by annealing in air, as an efficient approach to obtain Ni based gas diffusion electrodes functionalized with IrO_x. The reaction mechanisms have been investigated, and an optimal condition has been reached, obtaining an electrode with overpotential of 360 mV at 10 mA cm^{-2}, while keeping low the amount of noble metal loading, in the range of few μg cm^{-2}. Results are very promising in terms of electrode performance and stability.

Experimental section

Materials and preparation

The electroless deposition of iridium on Ni has been obtained by immersion in aqueous solution containing H_2IrCl_6. All the samples were dipped in the same volume of the deposition solution, 50 ml, containing 1 mM of H_2IrCl_6, 1 mM HCl and 2 mM KOH. Depositions were performed by stirring the solution at 600 rpm and by adding Isopropyl Alcohol (C_3H_8O IPA) at a concentration of 5%. The immersion time varied from 10 min to 120 min. After deposition, the samples were rinsed in deionized water, dried with N_2 and then annealed in air for 3 h at 250 °C to obtain Ir oxidation. Two different Ni substrates were used: flat Ni and Ni foam.

Flat Ni film, 150 nm thick, was deposited by sputtering on a silicon (100) substrate and functionalized with Ir, as previously described. Before the deposition the Ni film surface was cleaned by dipping for 10s in HCl 10 mM at RT. Ni foam (1.6 mm thick, porosity of 95%) with a pore density of 20p cm^{-1}, was purchased by Goodfellow. Electrodes of 4 × 1 cm^2 were cut and sonicated for 10 min in acetone at

60 °C. After rinsing, the native oxide was etched in HCl 10 mM at 60 °C for 30 min.

After cleaning, the samples were immersed in the Ir-based solution for deposition and subsequently rinsed, dried and annealed.

Characterization

The X-ray photoelectron spectroscopy (XPS) has been employed to study the chemical composition of the samples after immersion in the Ir deposition solution and subsequent annealing. XPS spectra were acquired with a PHI 5600 multi-technique ESCA-Auger spectrometer equipped with a standard Mg Kα X-ray source. Samples were analyzed with a photoelectron take-off angle of 45° (relative to the sample surface) and with an acceptance angle of ±7°. The XPS binding energy scale was referenced by centering the C 1s peak at 285.0 eV.

The morphology of Ni flat samples functionalized with Ir has been studied by Transmission Electron Microscopy (TEM) and by HAADF (High Angle Annular Dark Field) STEM with a Sub Angstrom JEOL STEM Cs-corrected ARM 200F equipped with a large area (100 mm^2) Silicon Drift Detector for Energy Dispersive X-Ray (EDX) analyses.

Scanning Electron Microscopy (SEM) using a ZEISS FE-SEM SUPRA 35 equipped with an Energy Dispersive X-ray (EDX) microanalysis system (X-MAX, 80 mm^2 by Oxford Instruments) has been employed to study the morphology of Ni foam samples. The amount of Ir deposited on the Ni foam was determined by EDX with beam energy of 15 keV in top view configuration.

Electrochemical measurements

The electrochemical measurements of Ni foam electrodes have been performed by using a Keithley 2600-Source Current Unit. The working electrode has been tested using a three electrodes setup with a Pt wire as counter electrode (CE) and a saturated calomel electrode (SCE, saturated KCl) as reference. The anodic oxygen evolution reaction (OER) has been investigated by linear sweep voltammetry (LSV). Untreated Ni foam and foam functionalized with IrO_x have been compared. The electrolyte was KOH 1.0 M and the experiments were performed at room temperature, under ambient light.

Tafel analyses were performed using the same three electrodes setup in a quasi-steady state condition, achieved by applying a sweeping rate of 0.1 mV s^{-1}. The electrochemical active area was estimated by cyclic voltammetry, recorded in a non-faradic potential window between 1.17 V and 1.27 V vs RHE, at scan rates of 10-20-30-47-57 mV s^{-1}.

The stability of the samples was tested in a two electrodes cell at a distance of 2 mm, in which Ni foam loaded with 15 μg cm^{-2} of Pt is employed as electrode for the hydrogen evolution reaction and: i) unmodified Ni foam or ii) IrO_x functionalized Ni foam, as OER. The two electrodes have the same area. Constant current stress was performed at a current density of 50 mA cm^{-2}.

All the potential values measured vs SCE were calibrated to RHE according to equation E (RHE) = E (SCE) + 0.244 V + 0.059 × pH.

Results and discussion

The preparation of the samples is schematically shown in Fig. 1. After cleaning, the Ni substrate (either foam or flat film on Si) was immersed in the solution with Ir and then annealed at 250 °C for 3 h in air.

The color of the as prepared solution is dark brown but it changes from light yellow to colorless, thus indicating a depletion of ($IrCl_6$) ion species as shown in Fig. 1. The spontaneous reaction for Ir deposition occurring between the $(IrCl_6)^{-2}$ and the Ni substrate is expected to be [53]:

$$(IrCl_6)^{2-} + 2\ Ni \rightarrow Ir + 2Ni^{2+} + 6\ Cl^{-} \quad (1)$$

Other possible reactions can be:

$$2\ (IrCl_6)^{2-} + Ni \rightarrow 2\ (IrCl_6)^{3-} + Ni^{2+} \quad (2)$$

Or

$$2\ (IrCl_6)^{2-} + 12H_2O + Ni \rightarrow 2\ [Ir(OH)_6]^{3-} + Ni^{2+} + 12\ HCl \quad (3)$$

Only reaction (1) gives rise to the deposition of metallic Ir, while for the other processes the presence of $(IrCl_6)^{2-}$ ions or $[Ir(OH)_6]^{3-}$ is expected. In order to verify which reaction takes place, as deposited and annealed samples have been studied by XPS.

Fig. 2(a-b) shows the XPS spectra of flat Ni film functionalized by 10 min deposition in the Ir-based solution. The spectra of the same sample after annealing at 250 °C for 3 h are shown in Fig. 2(c–d). The relative composition of Ir and Cl in the as deposited sample is 1:7 (see Fig. S1), suggesting that $IrCl_x$ ions are adsorbed on the Ni foam (reaction (2)), without the formation of metallic Ir. For the Ir 4f region, two spin-orbit peaks are observed in the spectrum of the as deposited sample (Fig. 2(a)): 4f 7/2 and 4f 5/2, located at 62.2 eV and 65.0 eV, respectively, indicating the +3 oxidation state of Ir, typical of $IrCl_x$ [54].

Upon annealing the Ir 4f 7/2 and 4f 5/2 peaks (Fig. 2(c)) shift to 61.7 eV and 64.91 eV [55], respectively, indicating the increase of the oxidation state towards the state +4 of Ir in IrO_x [56]. In Fig. 2(a), close to the Ir 4f peaks, the Ni 3p peak and its satellite are detected at 67.2 eV and 72 eV, respectively. No change is observed upon annealing (Fig. 2(c)). The Ni 2p 3/2 and 2p 1/2 components are also detected, together with the corresponding satellite peaks, as shown in Fig. 2(b–d) for as deposited and annealed samples, respectively. The peak at 855.0 eV can be ascribed to Ni +2 and the peak at 856.9 eV is related to the oxidation state +3 of Ni, suggesting the presence of both NiO and NiOOH. The O 1s region, shown in Fig. S2 before and after annealing, has been deconvoluted in three peaks, that can be assigned to metallic oxide species (Ir/Ni–O at about 530.2 eV), metallic hydroxide (mainly NiOOH at about 532.2 eV), and the absorbed water on the surface (H–O–H at about 533.3 eV). From these chemical analyses we can conclude that in the as prepared sample, $IrCl_x$ ions are deposited on the Ni surface, which is oxidised, with the formation of NiO and NiOOH. Upon annealing, the oxidation state of Ir increases from +3 to a value closer to +4 and the

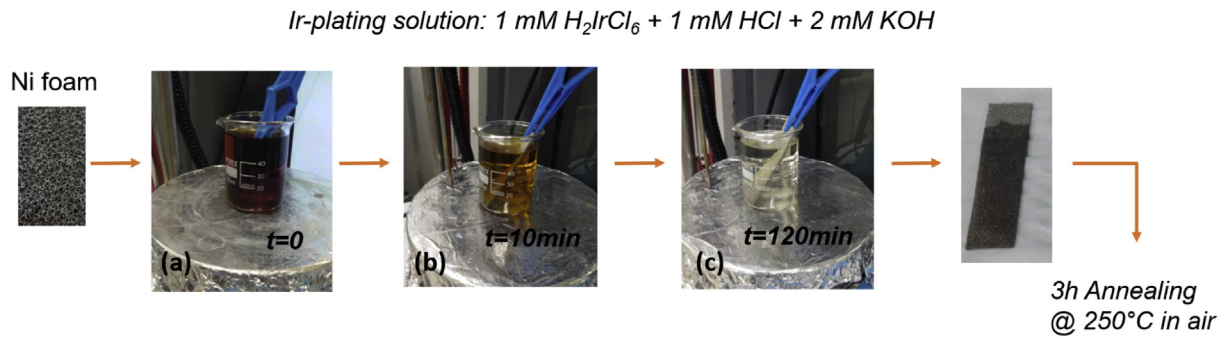

Fig. 1 – Schematic of the fabrication process of Ni foam functionalized with IrO_x by electroless deposition and annealing.

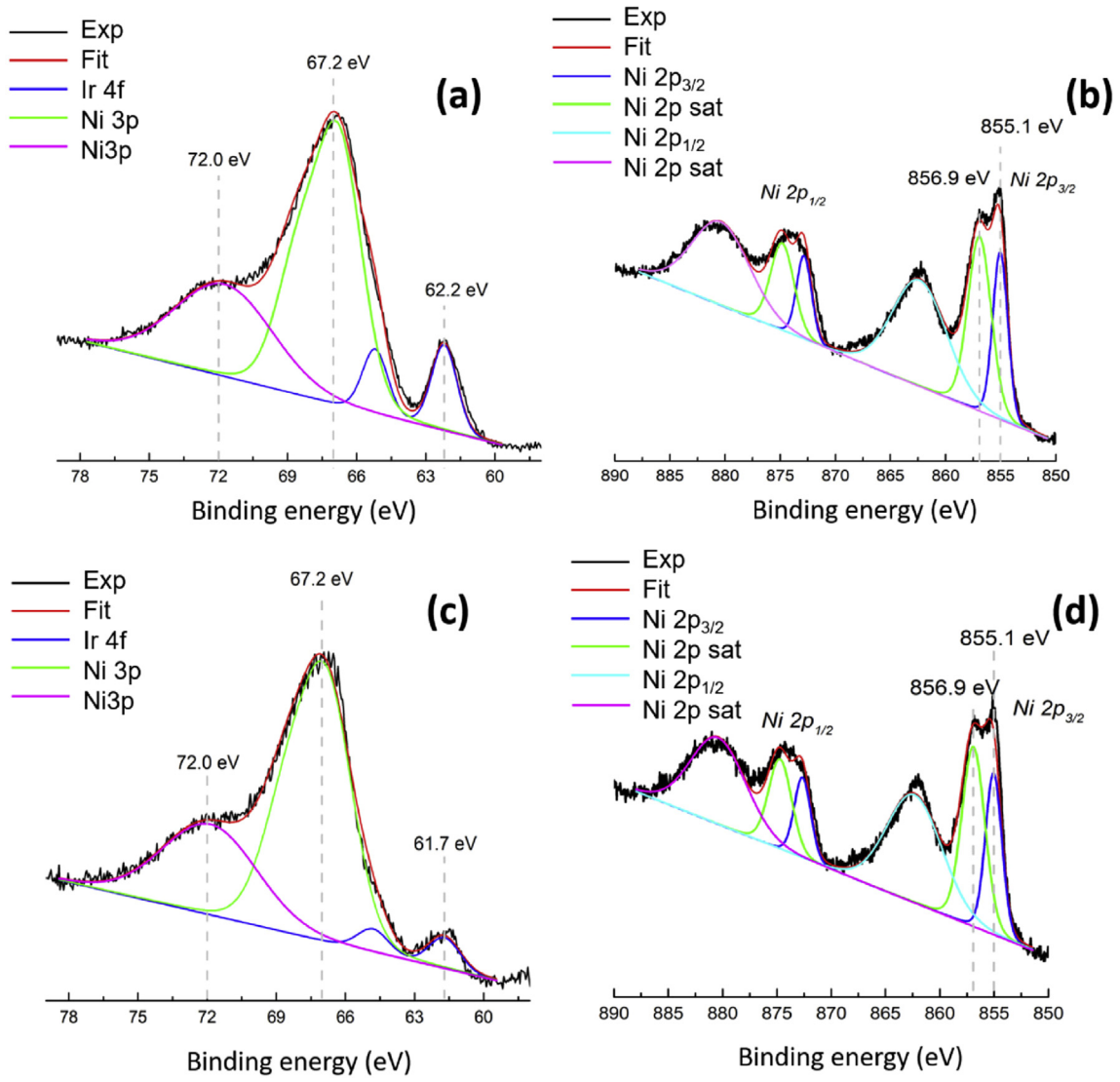

Fig. 2 – XPS spectra of as-deposited Ir on flat Nickel film, for 10 min deposition. (a) The Ir and Ni 3p regions and (b) the Ni 2p region; (c) and (d) the same sample, after annealing at 250 °C for 3 h.

amount of Cl is largely reduced (Fig. S1), therefore suggesting the formation of IrO_x. Correspondingly, the relative intensity of the O 1s peak at 530.2 eV (metallic oxide) increases. As expected, after annealing the signal related to the water absorbed on the surface almost disappears.

The same sample has been also analyzed by TEM microscopy before and after annealing, as shown in Fig. 3(a) and (b), respectively. The micrographs in plan view show the Ni crystalline grains, and small particles, with diameter around 2 nm. Fig. 3(c) and (d) show a high resolution TEM micrograph

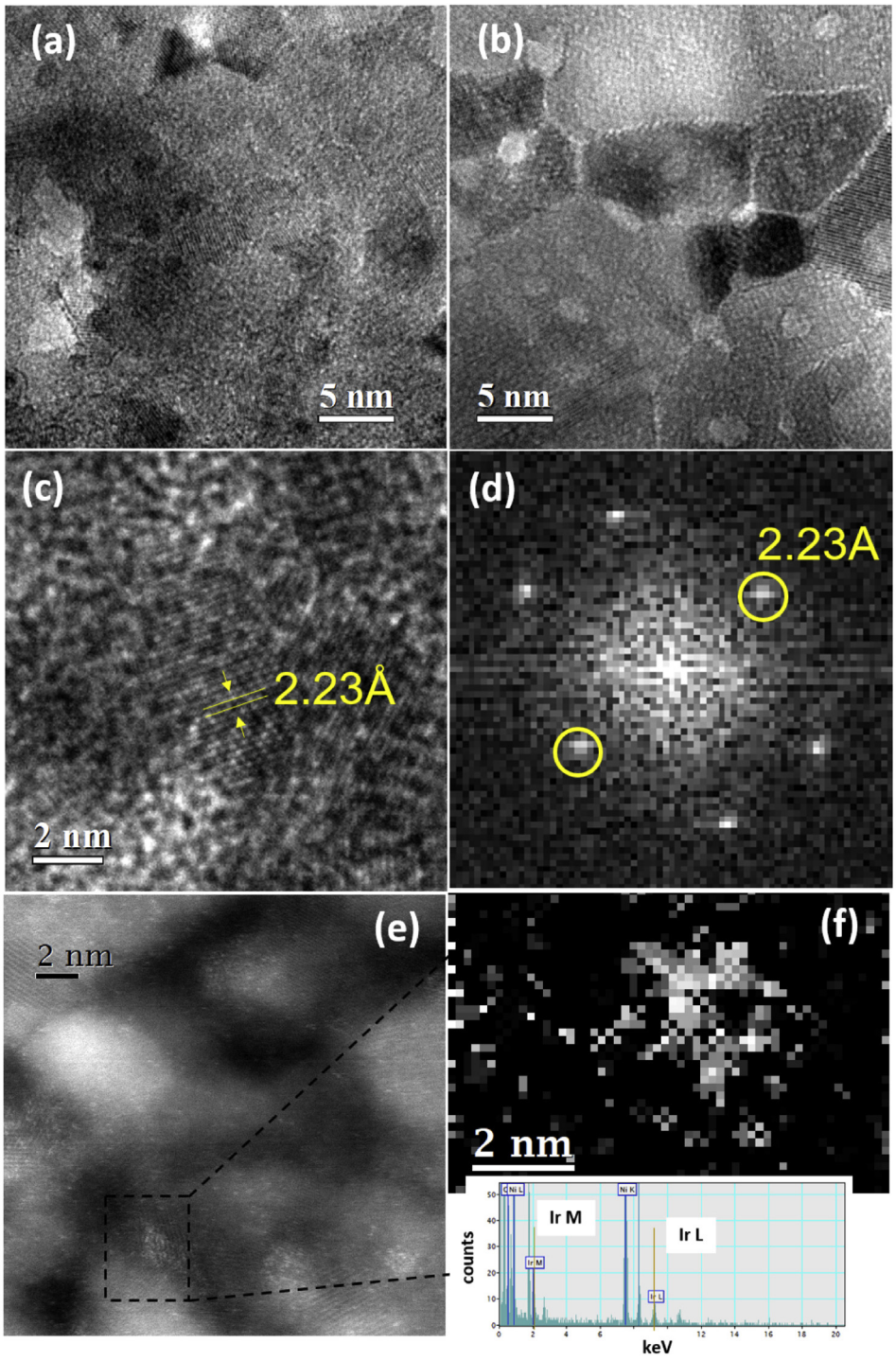

Fig. 3 – TEM micrograph in bright field of flat Ni functionalized with Ir by 10min deposition. (a) As prepared; (b) after annealing at 250 °C for 3 h; (c) HR TEM micrograph of the annealed sample showing the IrO_x nanoparticle; (d) the corresponding FFT; (e) HAADF- STEM with agglomeration of Ir atoms (brighter spots); (f) map of the Ir signal as acquired by EDX elemental analyses. EDX spectrum in the inset.

of an IrO_x nanoparticle and its Fast Fourier Transform (FFT), respectively. The measured lattice plane distance is 2.23 Å, corresponding to the (111) planes of IrO_x [57,58]. Scanning TEM (STEM) analysis performed in dark field of annealed sample (Fig. 3(e)) and EDX spectroscopy (see the inset in Fig. 3(f)), show that the brighter regions, with size of about 2 nm, contain Ir atoms. The Ir map acquired in the dashed region indicated in Fig. 3(e) is shown in Fig. 3(f).

Once we studied the deposition of Ir and the Ir oxide formation on flat Ni, we investigated the functionalization of the Ni foam. Fig. 4 (a) shows the XPS signal of the Ni 3p and Ir 4f peaks in Ni foam after Ir deposition by immersion for 30 min

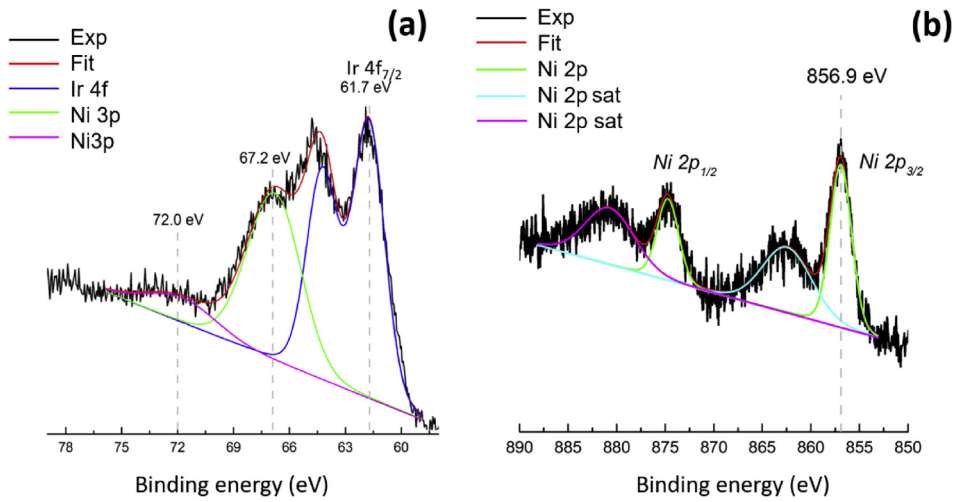

Fig. 4 – XPS signal of Ni foam sample after Ir deposition for 30 min and annealing at 250 °C for 3 h. (a) Ni 3p and Ir 4f peaks; (b) Ni 2p peaks.

and subsequent annealing at 250 °C for 3 h. As already observed for the flat Ni film, the Ir 4f 7/2 and 4f 5/2 peaks shown in Fig. 4(a) are shifted to 61.7eV and 64.91 eV, respectively, indicating an oxidation state of Ir close to +4, as in Ir oxide. Due to the longer deposition time (30 min) the amount of Ir, see Fig. S3 for quantification, is higher than observed in the flat sample (10 min deposition) and the residual Cl signal is very low. The Ni 3p region is not affected by the thermal treatment. The Ni 2p signal in Fig. 4(b) exhibits only one peak at 856.7 eV, corresponding to Ni 3+ (with satellite peaks at 862.4 eV and 880.4 eV), in contrast with the results obtained for flat Ni, in which both Ni+2 and Ni+3 signals have been detected. Such a result suggests the formation of NiOOH [59–62] rather than NiO in the 3D structured Ni foam. The O 1s region is shown in Fig. S4. On the surface mainly with Ni 3+ and Ir 4+ species have been found, corresponding to Ni hydroxide (signal at 532.5 eV) and IrO_x (the signal at 531.5eV) compounds.

The SEM micrographs of Ni foam after Ir deposition for 10min and annealing (250 °C 3 h) are shown in Fig. 5. The amount of Ir is very low, as verified by XPS (0.1 at%). The surface of the Ni foam does not show any relevant change in the morphology and the Ir loading is below the minimum amount detectable by the EDX system adopted in this study.

Fig. 6 shows the SEM micrograph obtained with a deposition time of 30 min. By increasing the immersion time, a larger amount of IrO_x was detected on the Ni foam. The SEM micrographs, coupled with EDX elemental map, highlight the presence of a thin layer with a wavelike structure (Ir ~1 wt%), localized on the outer surface of the Ni foam. We know that the performance of Ni foam electrodes is strictly related to the ability to achieve a coverage as homogeneous as possible also on the struts located in the inner part of the porous structure [52]. The analyses done on the inner regions are shown in Fig. S5. In this case, the surface morphology of the inner struts of the foam is quite smooth and doesn't show significant changes from that of uncovered Ni foam.

Fig. 7 shows the SEM micrographs of Ni foam sample immersed for 60 min in the Ir solution, and then annealed. The Ir amount, measured by EDX in that area is also reported. The wt % of Ir increased up to few units as shown in the spectrum of Fig. 7(d). Also, the inner regions are covered, as shown in S5.

Further increase of the deposition time up to 120 min produced very robust film with particles of several hundred nanometers in diameter and the same morphology has been found on the struts deep inside the foam (see Fig. S5). As a result, the apparent roughness seems to increase notably. The SEM micrographs are presented in Fig. 8 and the EDX spectra show Ir amount at the external surface of ~7 wt%. The same morphology has been found on the regions within the electrode (see Fig. S5).

Once the relative wt% amount of Ir is measured by EDX, however, the relevant information regarding the evaluation of the Ir loading into the electrode is not straightforward.

To evaluate the catalyst loading of a 1.6 mm thick Ni foam electrode, we have adopted the experimental procedure, described in Ref. [52], consisting in (i) embedding the Ni foam in an epoxy resin (ii) curing and cutting (iii) mechanically polishing with diamond paste. After such a preparation, the foam is observed by SEM in cross section to measure the thickness of the IrO_x layer covering the Ni foam (see Fig. S6). The amount of Ir can be then estimated by calculating first the fraction of total area filled by IrO_x, given by the thickness of the layer, multiplied by the external (measured) perimeter of the struts, and divided by the total investigated area. This ratio is then converted in volume fraction, as described in Ref. [52,63]. By considering the IrO_2 density (11.66 gr cm^{-3} [64]), the thickness can be converted in loading of the electrode (in g cm^{-2} of Ir). For a deposition time of 120 min, we measured an Ir oxide thickness varying between 100 nm and 25 nm, from the external to the internal regions. Such values correspond to an average Ir amount of 35 μg cm^{-2}. This value is extremely low when compared to the typical noble metal loading, for example employed in proton exchange membranes electrolyzers, of the order of 2 mg cm^{-2} [65–67].

The electrochemical activity of the Ni foam electrodes functionalized with Ir oxide has been tested by voltammetry

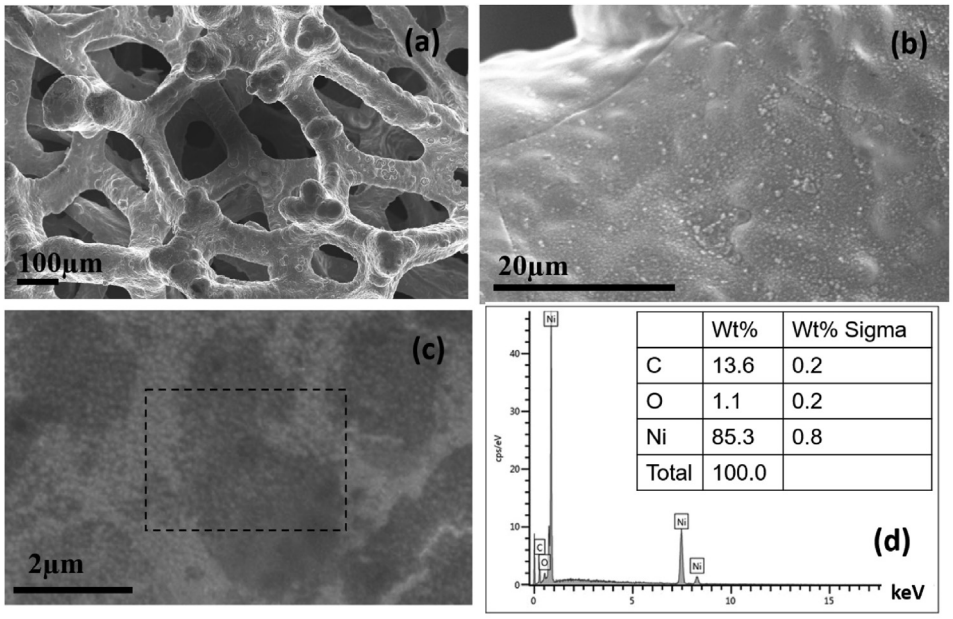

Fig. 5 – SEM micrograph of Ni foam after 10min Ir deposition and annealing. From (a) to (c) the surface is shown at increasing magnification. (d) EDX spectrum acquired in the external part of the foam, in the dashed rectangular region evidenced in (c), and showing only Ni, C and O signals.

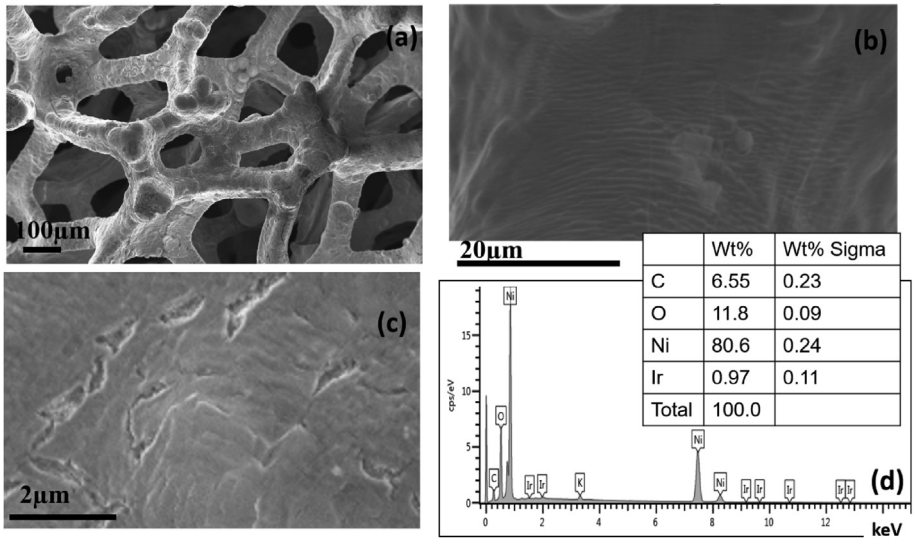

Fig. 6 – SEM micrograph of Ni foam after 30min Ir deposition and annealing. From (a) to (c) the surface is shown at increasing magnification. (d) EDX spectrum acquired in the outer region (like (c)) showing Ir signal.

measurements. First of all we compared the electrodes obtained after 10 min Ir deposition, without any annealing process, with bare Ni foam and with the same sample annealed at 250 °C for 3 h. As shown in Fig. 9(a), the annealed sample exhibits the lowest overpotential. The behavior of the electrodes under constant current stress of 50 mA cm^{-2} was also tested by monitoring the voltage in a two electrodes cell as a function of time. The electrode functionalized with Ir without annealing is not stable and the voltage continuously increases with time. At the end of the test, the color of the electrolyte solution changed into light yellow, similar to that shown in Fig. 1(b), therefore suggesting the dissolution of Ir in the KOH. We believe that such an instability is related to the fact that, as shown by XPS analyses, the adopted deposition technique gives rise to the deposition of $IrCl_x$ ions rather than metallic Ir. Such a condition seems to make the Ir/Ni foam catalyst not stable. We therefore focused on the electrochemical characterization of the annealed electrodes, with Ir oxide on Ni foam.

Voltammetry measurements have been performed by changing the sweep speed, as shown in Fig. 10(a)-(c) for some representative samples. The Tafel slopes, shown in Fig. 10(d), were calculated at the lowest sweep speed of 0.2 mV s^{-1}. For the nickel foam electrode the Tafel slope is 102 mV dec^{-1}. This value decreases to 47 mV dec^{-1} in the electrode functionalized

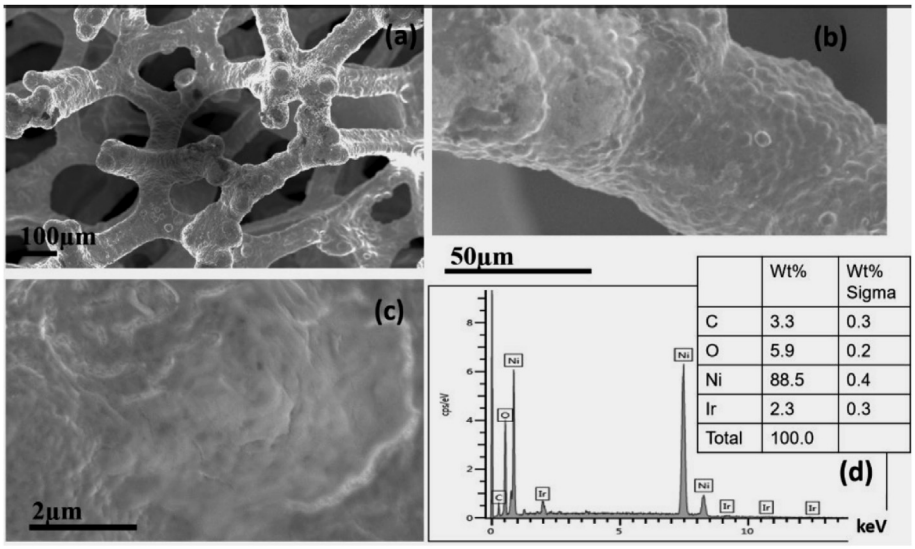

Fig. 7 – SEM micrographs of Ni foam functionalized by 60 min of IrO_x electroless deposition and annealing. (a–c) Images have been obtained at different magnification. (d) EDX spectrum acquired in a region like (c).

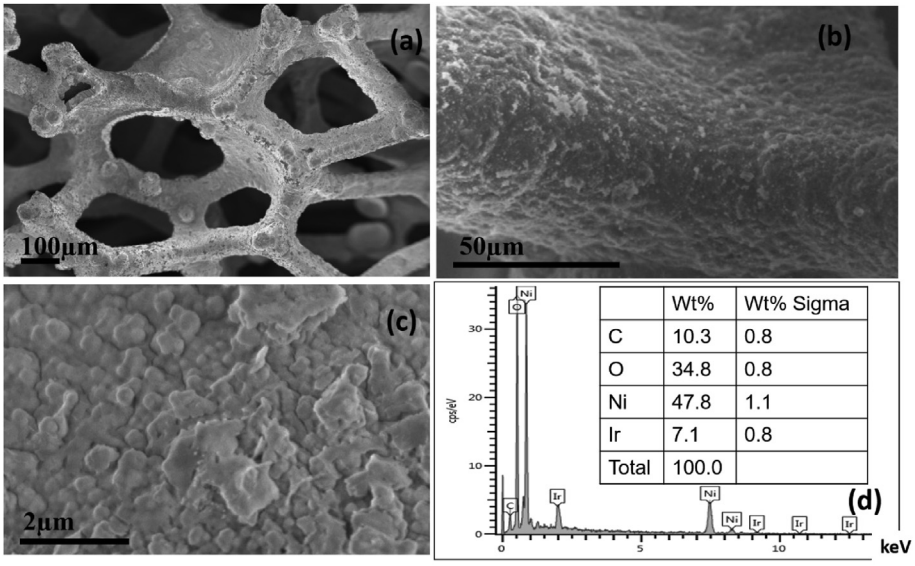

Fig. 8 – SEM micrographs of Ni foam with IrO_x after deposition for 120 min. (a–c) are obtained by increasing the magnification; (d) EDX spectrum acquired in a region like (c).

with IrO_x by 60min Ir deposition and to 38 mV dec^{-1} for the 120 min deposition, indicating a very efficient anodic transfer coefficient of about 0.27 [68].

For cyclic voltammetry measurements, we opted for a potential window that is, according to previous literature, associated with a change in the oxidation state of Ir^{3+} to Ir^{4+} and Ir^{4+} to Ir^{5+} [69,70]. Under these conditions, the capacitance can be calculated by plotting the current in the middle of the potential window as a function of the scan rate (the sweep speed in this case changed from 10 to 57 mV s^{-1}). This plot is a straight line with the slope given by the double layer capacitance [71], that is strictly related to the active area of electrocatalyst and thus to the number of active sites for the subsequent OER.

The data reported in Fig. 10 (e), are in agreement with previous findings [72] and indicate, for the sample obtained by 120 min Ir deposition, an increase in the capacitance by about one order of magnitude, compared to the bare Ni foam, suggesting the increase of the electrochemical active sites area. The results are summarized in Table 1.

Fig. 11(a) shows the overpotential of the studied electrodes, as calculated by the current voltage characteristics at 0.2 mV s^{-1}. The best performance, with overpotentials of 360 mV 10 mA cm^{-2}, 130 mV less than for bare Ni foam, is

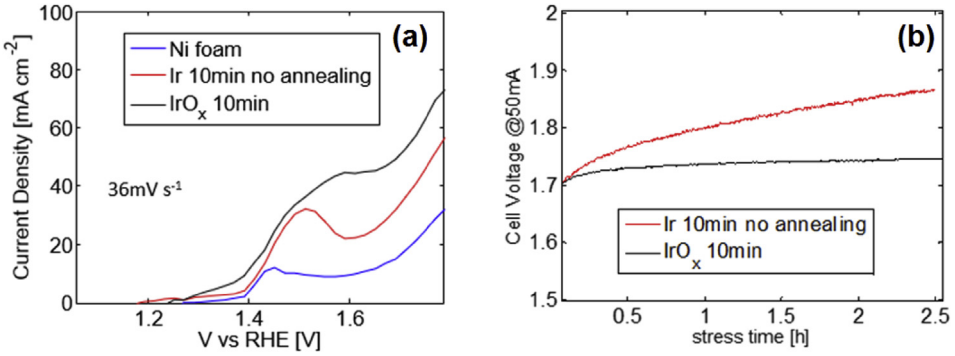

Fig. 9 – Comparison between an as deposited electrode, obtained after 10 min deposition time, and an electrode treated with the same procedure but annealed for 3 h at 250 °C in air: (a) Linear sweep voltammetry and (b) cell voltage under constant current stress of 50 mA cm^{-2}.

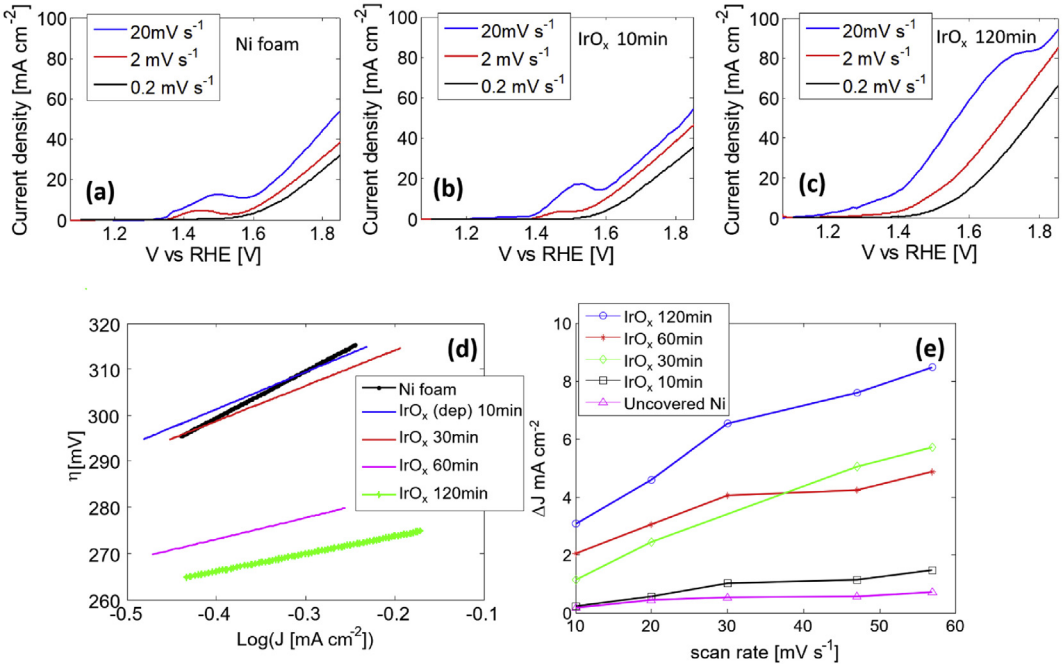

Fig. 10 – Electrochemical characterization of Ni foam electrodes functionalized with IrO_x: (a-b-c) Linear sweep voltammetry at different sweep speeds; (d) Tafel analysis; (e) double layer capacitance measurements.

Table 1 – Double layer capacitance and tafel slope measured for different samples.

	Ni foam	IrO_x 10 min	IrO_x 30 min	IrO_x 60 min	IrO_x 120 min
Capacitance [F]	9.61×10^{-3}	2.51×10^{-2}	9.68×10^{-2}	5.47×10^{-2}	1.12×10^{-2}
Tafel slope mV dec^{-1}	102	80	77	47	38

achieved with the electrode functionalized with a dipping of 120min in the plating bath.

In order to test the stability of the functionalized electrodes we used a two electrodes cell, employing the Ni foam functionalized with Ir oxide as OER and Ni foam functionalized with Pt as HER [52]. The cell voltage measured as a function of stress time under constant current operation (50 mA cm^{-2}) is reported in Fig. 11(b). The effectiveness of functionalization is evident, not only in terms of overvoltage reduction, but also of stability improvement. From results shown in Fig. 11, coupled together with the morphological analyses, it is evident that when the IrO_x is too low, leaving some uncovered internal Ni foam regions (Fig. S5), as in the sample with 10 min deposition (red solid line), not only the overvoltage is higher, but also the stability remains comparable to that of the bare Ni foam (black solid line). When the Ni coverage is complete, as verified for the 120 min sample, although the thickness is lower in the inner regions of the 3D structured electrode, the overvoltage is reduced and also the stability is largely improved (solid blue line).

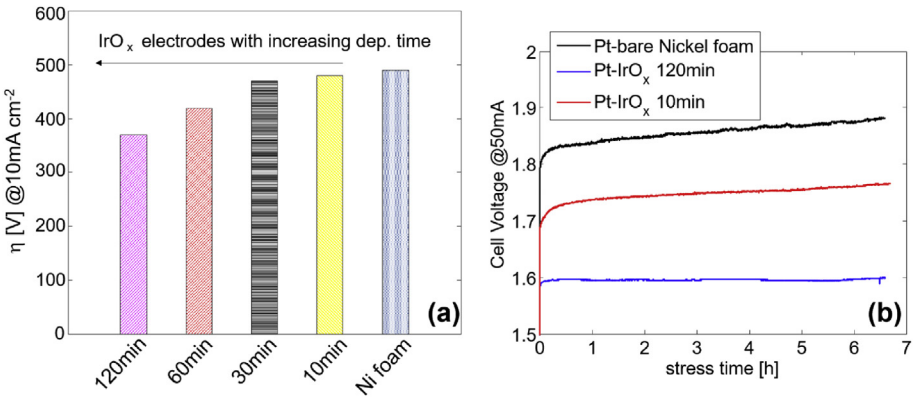

Fig. 11 – (a) Overpotential at 10 mA; (b) Two electrodes cell voltage as a function of time under constant current stress of 50 mA cm^{-2}.

Conclusions

Electroless deposition followed by annealing in air has been adopted as an advantageous strategy to functionalize nickel electrodes with IrO_x. The XPS analysis has elucidated that after deposition $IrCl_x$ species are found on the Ni surface. These species are not stable upon operation, while the annealing enables the formation of IrO_x and stabilizes the catalyst. Optimized deposition parameters allow optimal coverage of the nickel surface, as demonstrated by the morphological investigation by SEM. The electrochemical analyses have outlined the high catalytic activity, with an overvoltage of 360 mV. A very good electrode stability of Ir oxide has been also measured under constant current stress. The proposed deposition procedure is very promising since it allows low overpotential and good stability with extremely low Ir loading, of the order of 35 μg cm^{-2}.

Declaration of competing interest

The authors declare that they have no known competing financial interests or personal relationships that could have appeared to influence the work reported in this paper.

Acknowledgments

The work has been supported by the European Project PECSYS. The project has received funding from the Fuel Cells and Hydrogen 2 Joint Undertaking under grant agreement No 735218. This Joint Undertaking receives support from the European Union's Horizon 2020 Research and Innovation program and Hydrogen Europe and N. ERGHY.

Appendix A. Supplementary data

Supplementary data to this article can be found online at https://doi.org/10.1016/j.ijhydene.2020.07.049.

REFERENCES

[1] Hart R. Non-renewable resources in the long run. J Econ Dynam Contr 2016;71:1–20. https://doi.org/10.1016/j.jedc.2016.07.006.
[2] Lewis NS, Nocera DG. Powering the planet: chemical challenges in solar energy utilization. Proc Natl Acad Sci USA 2006;103:15729–35. https://doi.org/10.1073/pnas.0603395103.
[3] Cook TR, Dogutan DK, Reece SY, Surendranath Y, Teets TS, Nocera DG. Solar energy supply and storage for the legacy and nonlegacy worlds. Chem Rev 2010;110:6474–502. https://doi.org/10.1021/cr100246c.
[4] Bockris JOM. The hydrogen economy: its history. Int J Hydrogen Energy 2013;38:2579–88. https://doi.org/10.1016/J.IJHYDENE.2012.12.026.
[5] Schalenbach M, Tjarks G, Carmo M, Lueke W, Mueller M, Stolten D. Acidic or alkaline? Towards a new perspective on the efficiency of water electrolysis. J Electrochem Soc 2016;163(11):F3197–208. https://doi.org/10.1149/2.0271611jes.
[6] Zhou H, Yu F, Zhu Q, Sun J, Qin F, Yu L, Bao J, Yu Y, Chen S, Ren Z. Water splitting by electrolysis at high current densities under 1.6 volts. Energy Environ Sci 2018;11:2858. https://doi.org/10.1039/c8ee00927a.
[7] Sapountzi FM, Gracia JM, Weststrate CJ, Fredriksson HOA, Niemantsverdriet JW. Electrocatalysts for the generation of hydrogen, oxygen and synthesis gas. Prog Energy Combust Sci 2017;58:1–35. https://doi.org/10.1016/j.pecs.2016.09.001.
[8] Tijani AS, Yusup NAB, Rahim AHA. Mathematical modelling and simulation analysis of advanced alkaline electrolyzer system for hydrogen production. Procedia Technology 2014;15:798–806. https://doi.org/10.1016/j.protcy.2014.09.053.
[9] Schmidt O, Gambhir A, Staffell I, Hawkes A, Nelson J, Few S. Future cost and performance of water electrolysis: an expert elicitation study. Int J Hydrogen Energy 2017;42:30470–92. https://doi.org/10.1016/j.ijhydene.2017.10.045.
[10] Grigoriev SA, Fateev VN, Bessarabov DG, Millet P. Current status, research trends, and challenges in water electrolysis science and technology. Int J Hydrogen Energy 2020. https://doi.org/10.1016/j.ijhydene.2020.03.109. In press.
[11] Saleem MS, Abas N, Kalair AR, Rauf S, Haider A, Tahir MS, Sagir M. Design and optimization of hybrid solar-hydrogen generation system using TRNSYS. Int J Hydrogen Energy 2020;45:15814–30.
[12] Jafari M, Armaghan D, Mahmoudi SMS, Chitsaz A. Thermoeconomic analysis of a standalone solar hydrogen system with hybrid energy storage. Int J Hydrogen Energy 2019;44:19614–27.

[13] Kong H, Kong X, Wang H, Wang J. A strategy for optimizing efficiencies of solar thermochemical fuel production based on nonstoichiometric oxides. Int J Hydrogen Energy 2019;44:19585–94.
[14] Zeng K, Zhang D. Recent progress in alkaline water electrolysis for hydrogen production and applications. Prog Energy Combust Sci 2010;36:307–26. https://doi.org/10.1016/j.pecs.2009.11.002.
[15] Carmo M, Fritz DL, Mergel J, Stolten D. A comprehensive review on PEM water electrolysis. Int J Hydrogen Energy 2013;38:4901–34. https://doi.org/10.1016/j.ijhydene.2013.01.151.
[16] Grigoriev SA, Porembsky VI, Fateev VN. Pure hydrogen production by PEM electrolysis for hydrogen energy. Int J Hydrogen Energy 2006;31(2):171–5. https://doi.org/10.1016/j.ijhydene.2005.04.038.
[17] Pletcher D, Li X. Prospects for alkaline zero gap water electrolyzers for hydrogen production. Int J Hydrogen Energy 2011;23(36):15089–104. https://doi.org/10.1016/j.ijhydene.2011.08.080.
[18] Song S, Zhang H, Ma X, Shao Z, Baker RT, Yi B. Electrochemical investigation of electrocatalysts for the oxygen evolution reaction in PEM water electrolyzers. Int J Hydrogen Energy 2008;33(19):4955–61. https://doi.org/10.1016/j.ijhydene.2008.06.039.
[19] Antolini E. ACS Catal 2014;4(5):1426–40. https://doi.org/10.1021/cs4011875.
[20] Opaka D, Scheurer C, Reuter K. Ab initio thermodynamics insight into the structural evolution of working IrO_2 catalysts in proton-exchange membrane electrolyzers. ACS Catal 2019;9:4944–50. https://doi.org/10.1021/acscatal.9b00796.
[21] Cheng H, Li WL, Yang ZP. Enhancement of hydrogen evolution reaction by Pt nanopillar-array electrode in alkaline media and the effect of nanopillar length on the electrode efficiency. Int J Hydrogen Energy 2019;44:30141–50.
[22] Xie L, Qu F, Liu Z, Ren X, Hao S, Ge R, Du G, Asiri AM, Sun X, Chen L. In situ formation of a 3D core/shell structured Ni3N@Ni–Bi nanosheet array: an efficient non-noble-metal bifunctional electrocatalyst toward full water splitting under near-neutral conditions. J Mater Chem A 2017;5:7806–10.
[23] Yang L, Ren X, Wang Z, Liu Z, Du G, Asiri AM, Yao Y, Sun X. Hierarchical $CuCo_2S_4$ nanoarrays for high-efficient and durable water oxidation electrocatalysis. Chem Commun 2018;54:78–81.
[24] Tang C, Zhang R, Lu W, Wang Z, Liu D, Hai S, Du G, Asiri AM, Sun X. Energy-saving electrolytic hydrogen generation: Ni 2 P nanoarray as a high-performance non-noble-metal electrocatalyst. Angew Chem Int Ed Engl 2017;56:842–6.
[25] Ge R, Ma M, Ren X, Qu F, Liu Z, Du G, Asiri AM, Chen L, Zheng B, Sun X. A $NiCo_2O_4$@Ni–Co–Ci core–shell nanowire array as an efficient electrocatalyst for water oxidation at near-neutral pH. Chem Commun 2017;53:7812–5.
[26] Liu Q, Xie L, Liu Z, Du G, Asiri AM, Sun X. A Zn-doped Ni_3S_2 nanosheet array as a high-performance electrochemical water oxidation catalyst in alkaline solution. Chem Commun 2017;53:12446–9.
[27] Fuel cell technologies office. Multi-year research, D., and demonstration plan http://energy.gov/sites/prod/files/2016/10/f33/fcto_myrdd_fuel_cells.pdf.
[28] Zhu W, Zhang R, Qu F, Asiri AM, Sun X. Design and Application of Foams for Electrocatalysis. ChemCatChem 2017;9:1721–43. https://doi.org/10.1002/cctc.201601607.
[29] Chaudhari NK, Jin H, Kim B, Lee K. Nanostructured materials on 3D nickel foam as electrocatalysts for water splitting. Nanoscale 2017;9:12231–47. https://doi.org/10.1039/C7NR04187J.
[30] Wang T, Zhang X, Zhu X, Liu Q, Lu S, Asiri AM, Luo Y, Sun X. Hierarchical CuO@ZnCo LDH heterostructured nanowire arrays toward enhanced water oxidation electrocatalyst. Nanoscale 2020;12:5359–62.
[31] Lu W, Liu T, Xie L, Tang C, Liu D, Hao S, Qu F, Du G, Ma Y, Asiri AM, Sun X. In situ derived Co–B nanoarray: a high-efficiency and durable 3D bifunctional electrocatalyst for overall alkaline water splitting. Small 2017;13:1700805.
[32] Eftekhari A. Tuning the electrocatalysts for oxygen evolution reaction. Mater Today Energy 2017;5:37–57. https://doi.org/10.1016/j.mtener.2017.05.002.
[33] Ji X, Zhang R, Shi X, Asiri AM, Zheng B, Sun X. Fabrication of hierarchical CoP nanosheet@microwire arrays via space-confined phosphidation toward high-efficiency water oxidation electrocatalysis under alkaline conditions. Nanoscale 2018;10. 7941-7045.
[34] Li P, Zhao R, Chen H, Wang H, Wei P, Huang H, Liu Q, Li T, Shi X, Zhang Y, Liu M, Sun X. Recent advances in the development of water oxidation electrocatalysts at mild pH. Small 2019;15:1805103.
[35] You C, Ji Y, Liu Z, Xiong X, Sun X. Ultrathin CoFe-borate layer coated CoFe-layered double hydroxide nanosheets array: a non-noble-metal 3D catalyst electrode for efficient and durable water oxidation in potassium borate. ACS Sustainable Chem Eng 2018;6:1527–31.
[36] Yang L, Xie L, Ren X, Wang Z, Liu Z, Du G, Asiri AM, Yao Y, Sun X. Hierarchical $CuCo_2S_4$ nanoarrays for high-efficient and durable water oxidation electrocatalysis. Chem Commun 2014;54:78–81.
[37] Lee Y, Suntivich J, May KJ, Perry EE, Shao-Horn Y. Synthesis and activities of rutile IrO_2 and RuO_2 nanoparticles for oxygen evolution in acid and alkaline solutions. J Phys Chem Lett 2012;3:399–404. https://doi.org/10.1021/jz2016507.
[38] Osaka A, Takatsuna T, Miura Y. Iridium oxide films via sol-gel processing. J Non-Cryst Solids 1994;178:313–9. https://doi.org/10.1016/0022-3093(94)90300-X.
[39] Lv H, Zhanga G, Hao C, Mi C, Zhou W, Yang D, Li B, Zhang C. Activity of IrO_2 supported on tantalum-doped TiO_2 electrocatalyst for solid polymer electrolyte water electrolyzer. RSC Adv 2017;7:40427–36. https://doi.org/10.1039/C7RA06534E.
[40] Karthik PE, Raja KA, Kumar SS, Phani KLN, Liu Y, Guo SX, Zhang J, Bond AM. Electroless deposition of iridium oxide nanoparticles promoted by condensation of $[Ir(OH)_6]^{2-}$ on an anodized Au surface: application to electrocatalysis of the oxygen evolution reaction. RSC Adv 2015;5:3196–9. https://doi.org/10.1039/C4RA14392B.
[41] Zhao Y, Vargas-Barbosa NM, Hernandez-Pagan EA, Mallouk TE. Anodic deposition of colloidal iridium oxide thin films from hexahydroxyiridate(IV) solutions. Small 2011;7(14):2087–93. https://doi.org/10.1002/smll.201100485.
[42] El Sawy EN, Birss VI. Nano-porous iridium and iridium oxide thin films formed by high efficiency electrodeposition. J Mater Chem 2009;19:8244–52. https://doi.org/10.1039/b914662h.
[43] Elsen HA, Monson CF, Majda M. Effects of electrodeposition conditions and protocol on the properties of iridium oxide pH sensor electrodes. J Electrochem Soc 2009;1:156. https://doi.org/10.1149/1.3001924. F1-F6.
[44] Etenko A, McKechnie T, Shchetkovskiy A, Smirnov A. Oxidation-protective iridium and iridium-rhodium coating produced by electrodeposition from molten salts. ECS Transactions 2007;14(3):151–7. https://doi.org/10.1149/1.2721466.
[45] Yeh BP, Lisker M, Bläsing J, Khorkhordin O, Kalkofen B, Burte EP. Deposition of iridium thin films on three-dimensional structures with PE-MOCVD. Chem Vap Depos 2015;21:46–53. https://doi.org/10.1002/cvde.201407133.
[46] Maury F, Senocq F. Iridium coatings grown by metal–organic chemical vapor deposition in a hot-wall CVD reactor. Surf

Coating Technol 2013;163–164:208–13. https://doi.org/10.1016/S0257-8972(02)00485-1.
[47] Xu C, Baum TH. New precursors for chemical vapor deposition of iridium. Chem Mater 1998;10(9):2329–31. https://doi.org/10.1021/cm980346x.
[48] Dey SK, Goswami J, Wang CG, Majhi P. Preparation of iridium films by liquid source metalorganic chemical vapor deposition. Jpn J Appl Phys 1999;38:L1052. https://doi.org/10.1143/JJAP.38.L1052.
[49] Slavcheva E, Radev I, Bliznakov S, Topalov G, Andreev P, Budevski E. Sputtered iridium oxide films as electrocatalysts for water splitting via PEM electrolysis. Electrochim Acta 2007;12(52):3889–94. https://doi.org/10.1016/j.electacta.2006.11.005.
[50] El Khakani MA, Chaker M, Le Drogoff B. Sputtered iridium oxide films as electrocatalysts for water splitting via PEM electrolysis. J Vac Sci Technol A 1998;16:885. https://doi.org/10.1116/1.581029.
[51] Mattinen M, Hämäläinen J, Vehkamäki M, Heikkilä MJ, Mizohata K, Jalkanen P, Räisänen J, Ritala M, Leskelä M. Atomic layer deposition of iridium thin films using sequential oxygen and hydrogen pulses. J Phys Chem C 2016;28(120):15235–43. https://doi.org/10.1021/acs.jpcc.6b04461.
[52] Milazzo RG, Privitera SMS, D'Angelo D, Scalese S, Di Franco S, Maita F, et al. Spontaneous galvanic displacement of Pt nanostructures on nickel foam: synthesis, characterization and use for hydrogen evolution reaction. Int J Hydrogen Energy 2018. https://doi.org/10.1016/j.ijhydene.2018.03.042.
[53] Mellsop SR, Gardiner A, Marshall AT. Spontaneous deposition of iridium onto nickel substrates for the oxygen evolution reaction. Electrocatalysis 2016;7:226–34.
[54] Hüppauff M. Valency and structure of iridium in anodic iridium oxide films. J Electrochem Soc 1993;140:598. https://doi.org/10.1149/1.2056127.
[55] NIST XPS database https://srdata.nist.gov/xps/Default.aspx;.
[56] Rubel M, Haasch R, Mrozek P, Wieckowski A, De Pauli C, Trasatti S. Characterization of IrO_2/SnO_2 thin layers by electron and ion spectroscopies. Journal of Vacuum 1994;45:423. https://doi.org/10.1016/0042-207X(94)90314-X.
[57] Lettenmeier P, Wang L, Schindler UG, Gazdzicki P. Nanosized IrO_x–Ir catalyst with relevant activity for anodes of proton exchange membrane electrolysis produced by a cost-effective procedure. Angew Chem Int Ed 2016;55:742–6.
[58] Bestaoui N, Prouzet E, Deniard P, Brec R. Structural and analytical characterization of an iridium oxide thin layer. Thin Solid Films 1993;235:35–42.
[59] Weidler N, Schuch J, Knaus F, Stenner P, Hoch S, Maljusch A, et al. X-ray photoelectron spectroscopic investigation of plasma-enhanced chemical vapor deposited NiO_x, $NiO_x(OH)_y$, and $CoNiO_x(OH)_y$: influence of the chemical composition on the catalytic activity for the oxygen evolution reaction. J Phys Chem C 2017;121:6455–63.
[60] Grosvenor AP. New interpretations of XPS spectra of Nickel metal and oxides. Surf Sci 2006;600:1771–9.
[61] Mc Intyre NS, Cook MG. Anal Chem 1975;47:13.
[62] Carley AF, et al. The formation and characterization of Ni^{3+}-an X-ray photoelectron spectroscopic investigation of potassium-doped Ni(110)–O. Surf Sci 1999;440:L868–74.
[63] Milazzo RG, Privitera SMS, Scalese S, Lombardo S. Effect of morphology and mechanical stability of nanometric platinum layer on nickel foam for hydrogen evolution reaction. Energies 2019;12:16. https://doi.org/10.3390/en12163116.
[64] https://materialsproject.org/materials/mp-2723/;.
[65] Jia J, Seitz LC, Benck JD, Huo Y, Chen Y, Desmond JW. Solar water splitting by photovoltaic-electrolysis with a solar-to-hydrogen efficiency over 30%. Nat Commun 2016;7:13237. https://doi.org/10.1038/ncomms13237.
[66] Burgess G, Fernandez-Velasco JG. Materials, operational energy inputs, and net energy ratio for photo biological hydrogen production. Int J Hydrogen Energy 2007;32:1225–34. https://doi.org/10.1016/j.ijhydene.2006.10.055.
[67] Ganley JC. High temperature and pressure alkaline electrolysis. Int J Hydrogen Energy 2009;34:3604–11. https://doi.org/10.1016/j.ijhydene.2009.02.083.
[68] Hüppauff M. Valency and structure of iridium in anodic iridium oxide films. J Electrochem Soc 1993;140:598. https://doi.org/10.1149/1.2056127.
[69] Juodkazyte J, Sebeka B, Valsiunas I, Kestutis J. Iridium anodic oxidation to Ir(III) and Ir(IV) hydrous oxides. Electroanalysis 2005;17:11. https://doi.org/10.1002/elan.200403200.
[70] Grupioni A, Arashiro E, Lassali T. Voltammetric characterization of an iridium oxide-based system: the pseudocapacitive nature of the $Ir_{0.3}Mn_{0.7}O_2$ electrode. Electrochim Acta 2002;48:407–18. https://doi.org/10.1016/S0013-4686(02)00686-2.
[71] Transatti S. Physical electrochemistry of ceramic oxides. Electrochim Acta 1991;36:225–41.
[72] Ardizzone S, Carugati A, Trasatti S. Surface structure of ruthenium dioxide electrodes and kinetics of chlorine evolution. J Electrochem Soc 1982;129:1689.